ENGINEERING

Capillary-driven desalination in a synthetic mangrove

Yunkun Wang[1,2], Jongho Lee[2,3], Jay R. Werber[2,4], Menachem Elimelech[2]*

Copyright © 2020 The Authors, some rights reserved; exclusive licensee American Association for the Advancement of Science. No claim to original U.S. Government Works. Distributed under a Creative Commons Attribution NonCommercial License 4.0 (CC BY-NC).

According to the cohesion-tension theory, mangrove trees desalinate salty water using highly negative pressure (or tension) that is generated by evaporative capillary forces in mangrove leaves. Here, we demonstrate a synthetic mangrove that mimics the main features of the natural mangrove: capillary pumping (leaves), stable water conduction in highly metastable states (stem), and membrane desalination (root). When using nanoporous membranes as leaves, the maximum osmotic pressures of saline feeds (10 to 30 bar) allowing pure water uptake precisely correspond to expected capillary pressures based on the Young-Laplace equation. Hydrogel-based leaves allow for stable operation and desalination of hypersaline solutions with osmotic pressures approaching 400 bar, fivefold greater than the pressure limits of conventional reverse osmosis. Our findings support the applicability of the cohesion-tension theory to desalination in mangroves, provide a new platform to study plant hydraulics, and create possibilities for engineered membrane separations using large, passively generated capillary pressures.

INTRODUCTION

Mangroves are salt-tolerant trees that grow in tropical and subtropical coastal regions around the world. To survive in their saline or brackish environments, mangroves tightly control water and ion uptake at the roots, enabling xylem saps to be nearly salt free (*1*–*3*). Salt exclusion is partially achieved by physical blockage of the nonselective apoplastic route, in which water and ions circumvent the cell membrane by moving through the cell walls of root cells (*1*, *4*). This blockage stems from the deposition of a waxy substance called suberin within the cell walls of endodermal cells, rendering the otherwise permeable cell walls essentially impermeable. Elimination of the apoplastic route results in uptake occurring primarily via the symplastic pathway, in which water and ions permeate the cell membrane and subsequently pass cell to cell through intracellular cytosol until entering the xylem for long-range transport. The cell membrane acts as the discriminating barrier. Ions are largely excluded from passive transport through the lipid bilayer, owing to the high solvation energy of ions in the hydrophobic core (*5*). Ions must therefore pass through selective pumps and channels, allowing the cell to control ion uptake. Water readily permeates the cell membrane, with the permeability of the membrane being enhanced by salt-excluding water channels called aquaporins (*6*). Owing to the selectivity of the cell membrane, salt exclusion in mangroves can reach up to 99% (*1*–*3*, *7*).

Water permeates the cell membrane by moving down its chemical potential gradient, which in mangrove trees is affected by salinity (osmotic pressure) and hydraulic pressure. That is, selective water transport through the cell membranes of mangrove roots is a form of reverse osmosis (RO), the main technology used industrially for desalination (*8*, *9*). As in industrial RO, water uptake at mangrove roots requires a hydraulic pressure difference greater than the osmotic pressure of the saline water in soil pores (e.g., seawater with an osmotic pressure of ~25 bar). Since the hydraulic pressure in soil has a maximum of ~1 bar (ambient pressure), mangrove trees must exert a negative pressure within the root cells, which has been observed experimentally for mangroves and other plants (*10*–*13*).

The cohesion-tension theory is well accepted to explain the mechanism of negative pressure generation in plants (*13*, *14*). An air-water interface (meniscus) is formed in channels within the cell walls of leaf mesophyll cells, equivalent to nanopores with diameters of O(10 nm) (*15*). With the meniscus at a relatively stationary position, water molecules removed by evaporation are replaced by water flow toward the meniscus. The cohesive force between water molecules ensures continuous water supply, which in turn generates a tension (negative pressure) between the molecules. The water surface tension of menisci formed in nanopores with a diameter of 20 nm can generate a negative pressure of −150 bar in xylems, root cells, and leaf cells (*14*, *16*). Such highly negative capillary pressures serve as the primary driving force for water transport in plants, for example, enabling water to reach ~100 m heights in giant sequoia trees (*14*, *17*).

Plants use the capillary pressure–driven mechanism to transport water over large distances and heights with minimal expenditure of chemical energy. The main energy input is instead passive heat absorption from the environment at the sites of evaporation. Inspired by this ability, exploitation of negative capillary pressures has recently been explored to achieve passive water transport in engineering applications, including ion chromatography, microfluidic pumping, and chemical concentration (*18*–*24*). These engineered devices have also allowed for controlled experiments to better understand complex plant hydraulics, for which much is still unknown (*25*, *26*). A major complication in plant hydraulics and in these engineered devices is the metastability of water under tension, as metastable water is prone to the formation of bubbles (cavitation) (*16*, *25*–*27*). For mangroves, the requirement of highly negative pressures to overcome the osmotic pressure of the surrounding saline water substantially increases the vulnerability to cavitation. Plants, including mangroves, have developed highly intricate structures to minimize cavitation and prevent embolism (blockage) of the xylem (*1*, *13*, *28*). In engineered systems, the challenge of maintaining bubble-free conduits has thus far limited capillary-driven fluidic transport to relatively low-pressure applications, typically less than 25 bar (the osmotic pressure of seawater). Furthermore, although mangrove-inspired membrane materials have been created (*23*, *29*), the negative-pressure–driven desalination of brackish and saline waters in mangroves, per the cohesion-tension theory, has not been mimicked

[1]Shandong Key Laboratory of Water Pollution Control and Resource Reuse, School of Environmental Science and Engineering, Shandong University, Qingdao 266237, China. [2]Department of Chemical and Environmental Engineering, Yale University, New Haven, CT 06520-8286, USA. [3]Department of Civil Engineering, University of British Columbia, Vancouver, British Columbia V6T 1Z4, Canada. [4]Department of Chemistry, University of Minnesota, Minneapolis, MN 55455-0431, USA.
*Corresponding author. Email: menachem.elimelech@yale.edu

Downloaded from http://advances.sciencemag.org/ on November 28, 2020

in a synthetic system. Demonstration of large, stable negative pressure in a synthetic system is needed to expand the potential use of capillary pressures to high-pressure engineering applications such as desalination, chemical purification, or chemical sensing.

In this work, we present a synthetic mangrove that captures the main features of natural mangrove trees: capillary pumping (leaves), water conduction from root to leaves in a highly metastable state (stem), and desalination (root). Specifically, the synthetic mangrove consists of a nanoporous anodized aluminum oxide (AAO) membrane or a poly(hydroxyethyl methacrylate)–based hydrogel as leaves, a porous fritted silica filter as the stem, and a polymeric RO membrane as the root. We demonstrate that the synthetic leaves can generate highly negative pressures that enable desalination through the RO membrane. Even under such highly metastable states, the synthetic mangrove maintains stable water uptake and desalination of saline water. Our work supports the cohesion-tension theory for desalination in mangroves and highlights the potential to use highly negative capillary pressures for diverse engineering applications.

RESULTS

Working principles of the synthetic mangrove

Design of the synthetic mangrove device sought to capture the essential features of transpiration and desalination in the mangrove tree. The main components are illustrated in Fig. 1 and fig. S1, with their natural analogs in the mangrove tree displayed as well. Desalination occurs at the root, which in the mangrove tree is the aquaporin-containing cell membrane. The synthetic mangrove uses a commercial, polymeric RO membrane that is designed for seawater desalination (SW30HR, Dow Water & Process Solutions). This membrane comprises a thin (<200 nm), dense polyamide selective layer on top of a porous support (*8*). Molecular transport across the selective layer is described by the solution-diffusion model, in which molecules sorb from the aqueous solution into the selective layer, diffuse down their concentration gradient, and then desorb into the aqueous phase on the other side (*30*, *31*). Solute (e.g., salt) flux, J_s, is mathematically similar to Fickian diffusion, with $J_s = B\Delta c$, where B is the solute permeability coefficient, and Δc is the difference in aqueous solute concentration across the membrane (*30*, *32*).

For water, a hydraulic pressure difference overcomes the difference in osmotic pressure to effect water flux, J_w (*30*, *32*)

$$J_w = A(\Delta P - \Delta\pi) = A\left[(P_o - P_{root}) - (\pi_o - \pi_{root})\right] \quad (1)$$

where A is the water permeability coefficient, and ΔP and $\Delta\pi$ are the hydraulic pressure and osmotic pressure differences across the membrane, respectively. In a mangrove root cell, these pressure differences are given by the hydraulic pressure, P_o, and osmotic pressure, π_o, of the soil pore water and the hydraulic pressure, P_{root}, and osmotic pressure, π_{root}, within the root cell. If water uptake is occurring (i.e., $J_w > 0$), then rearranging Eq. 1 yields the root hydraulic pressure

$$P_{root} < P_o - (\pi_o - \pi_{root}) \approx P_o - \pi_o \quad (2)$$

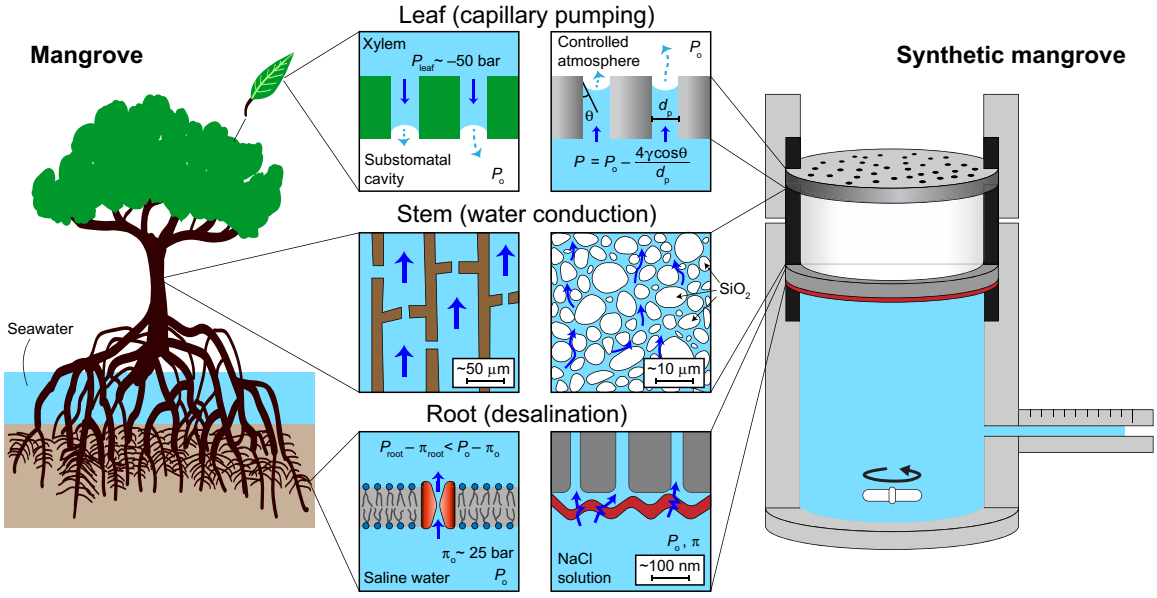

Fig. 1. Design elements and water flow in the synthetic mangrove. The schematic diagrams show the mangrove tree (left), the synthetic mangrove device (right), and their water transport mechanisms (center insets). In natural mangroves, capillary pressure created by evaporation into substomatal cavities (top left inset) brings about upward water transport through xylem channels (middle left inset) and desalination by aquaporin water channels in root cell membranes, which exclude salt from saline water in the soil (bottom left inset). The highly negative pressure in the root, P_{root}, overcomes the osmotic pressure of the saline water (π_o), which enables water uptake through the root filtration system (i.e., $P_{root} - \pi_{root} < P_o - \pi_o$). The synthetic mangrove as shown comprises a nanoporous AAO membrane, a silica frit, and an RO membrane, mimicking the leaf, stem, and root of natural mangrove trees, respectively. Negative capillary pressure in the nanopores of the AAO membrane (top right inset) is the driving force for water transport through the silica frit (middle right inset) and desalination of saline water by a semipermeable RO membrane (bottom right inset). Hydrogel membranes are also used as leaves. Membranes were sealed using rubber O-rings, shown in black. Magnetic stirring is used to enhance mixing of the saline feed water and minimize concentration polarization at the membrane surface. P_{leaf} and P_{root}, xylem sap pressure at the leaf and root, respectively; P_o, pressure in the soil or feed water; π_{root}, osmotic pressure of xylem sap at the root; π_o, osmotic pressure of soil or feed water (~25 bar for seawater); γ, water surface tension; θ, water contact angle on nanopore wall; d_p, nanopore diameter.

Downloaded from http://advances.sciencemag.org/ on November 28, 2020

Assuming high salt exclusion, π_{root} can be neglected. For natural mangroves, P_o is often negative due to capillary forces in the soil (*1*, *13*). In the synthetic mangrove, P_o is atmospheric pressure, as the solution in the feed reservoir is opened to air. The osmotic pressure of the feed, π_o, is therefore typically the main determinant of P_{root}. For example, with π_o of 25 bar for seawater, P_{root} must be lower than −24 bar to enable desalination in the root (Eq. 2). The osmotic pressure is a function of solute concentration and temperature. For low solute concentrations, the van't Hoff relation is commonly used to estimate the osmotic pressure: $\pi = ncR_gT$, where n is the van't Hoff factor (e.g., 2 for NaCl), c is the molar concentration of solute, R_g is the universal gas constant, and T is the absolute temperature. We used the OLI software (OLI systems, Hanover, NJ) to compute accurate values of π_o for a wide range of solute concentrations (up to 5 M NaCl).

The large negative pressures in mangrove roots originate from processes in the leaf, particularly capillary pressures generated upon the evaporation of water from fine, hydrophilic O(10 nm) pores in the cell walls of leaf mesophyll cells. Water evaporation results in the formation of a water-air interface (meniscus) with negative curvature. The corresponding pressure jump across the meniscus, $\Delta P_{w/a}$, can be estimated using the Young-Laplace equation (*5*, *13*)

$$\Delta P_{w/a} = \frac{4\gamma\cos\theta}{d_p} \quad (3)$$

where γ is the surface tension of water, θ is the water contact angle on the pore surface, and d_p is the pore diameter. From Eq. 3, for a water surface tension of 0.071 N m^{-1} at 30°C and θ ~ 0°, leaf cell nanopores with small pore sizes [$d_p \sim O$(10 nm)] can generate capillary pressures <−100 bar in the liquid phase. Plants also exhibit some control over the humidity within the substomatal cavity into which evaporation occurs, most notably by fully closing the opening (i.e., the stomata) of the cavity.

The synthetic mangrove utilized in this study used two types of leaves. The first were porous AAO membranes, which had relatively monodisperse pore diameters and were highly hydrophilic (i.e., low θ). These porous AAO membranes enabled mechanistic analysis of the generation of negative pressures, as the experimentally measured pore sizes could be included directly in Eq. 3. The second type of leaf was a hydrogel-filled macroporous membrane, wherein the hydrogel comprised cross-linked poly(2-hydroxyethyl methacrylate) or poly(HEMA). As discussed later, the hydrogel leaf enabled operation with greater stability, but the lack of pores complicates mechanistic analysis. To control the humidity, the synthetic mangrove was placed in a chamber with controlled temperature, humidity, and airflow.

In the natural mangrove, xylem vessels connect the leaves and roots, conducting desalinated water to the leaves and establishing negative pressures within the roots. Xylem vessels, formed from the cell walls of dead cells, have a complex physical structure to satisfy two main, somewhat conflicting, requirements (*13*). First, they must minimize the pressure drop from convective flow, which incentivizes large vessel diameters. Second, xylem vessels must preserve the metastable state of water under tension and thereby minimize cavitation (the formation of air bubbles). Physical mechanisms to minimize cavitation include relatively small vessel diameters within mangroves (compared to other plants), which are often <50 μm and decrease in size for increased soil salinity (*33*). In addition, each xylem vessel comprises a series of vertically and horizontally connected chambers, each formed from individual dead cells (*13*). This segmented structure enables cavitation events to be isolated, with only one chamber filling with air rather than the whole vessel network. Central to this safety mechanism are "pit membranes," which connect each chamber and have small hydrophilic O(10 nm) pores to stabilize water-air interfaces (by Eq. 3) between neighboring chambers in the event of cavitation (*13*, *26*, *34*). Such stabilization of the interface prevents air from filling neighboring chambers and eventually completely cutting off flow. The membrane connections additionally allow for fluid paths to circumvent the air-filled chamber.

As a relatively simple and easily accessible mimic of the xylem, the "stem" of the synthetic mangrove device was a 2.2-mm-thick silica frit with a nominal pore size of 0.9 to 1.4 μm (Fig. 1 and fig. S2). The glass frit lacks the structural complexity of the xylem, particularly the relatively large diameters of xylem vessels stabilized by the small pores of the pit membranes. Even so, the silica frit does mimic basic xylem features. The hydrophilicity of silica (low θ) combined with the ~1-μm pore size provides some stability against cavitation. The size distribution of the silica particles should also result in heterogeneous pore sizes that could stabilize entrapped air bubbles as in the xylem, albeit with less control and at smaller pressure differences. Last, the glass frit is highly permeable (see note S1), providing minimal resistance compared with the root (i.e., the RO membrane).

Water uptake and evaporation rates

We first consider pure water uptake to characterize evaporation from the synthetic mangrove leaf. In particular, using an AAO membrane with ~84-nm pores (table S1) as the leaf on top of the silica frit, we assessed the water evaporation rate and its dependence on humidity and temperature, mainly to ensure that our system allowed for proper control of the evaporation conditions. The evaporation rate was measured by the rate of change in the water level in the volumetric syringe (Fig. 1 and fig. S3) and was modeled by the convective mass transfer model for laminar flow on a flat surface (see note S2 and fig. S4). The results in Fig. 2A indicate that, as expected, humidity and temperature critically affect the evaporation rate. Increased bulk relative humidity decreases the water activity difference between the bulk and the air/water interface, resulting in reduced mass transfer driving force and, therefore, a reduced evaporation rate. Decreased temperature decreases the saturation vapor pressure, P_{vap}, which further decreases the evaporation rate. The evaporation rates in Fig. 2A were normalized to P_{vap}, with the normalized rates being largely similar for the different temperatures. Furthermore, the experimental evaporation rates followed the mass transfer model (note S2), with the model slightly underpredicting the evaporation rate, showing that conditions were well controlled in our system.

Evaporation was then characterized in the presence of the root RO membrane. As shown in Fig. 2B, the evaporation rates at 30°C and 40% relative humidity are essentially unchanged when the root membrane is present. That is, the resistance from the root membrane minimally affects transport when the feed solution is pure water. On the basis of Eq. 3, the 84-nm average pore diameter of the AAO membrane would yield a maximum negative pressure of −33 bar, assuming a minimum water contact angle (θ) of 12° (*35*, *36*). Using the water permeability coefficient of the RO membrane (2.7 ± 0.4 × 10^{-7} m s^{-1} bar^{-1}; see note S3 for measurement details) in Eq. 1, the

Downloaded from http://advances.sciencemag.org/ on November 28, 2020

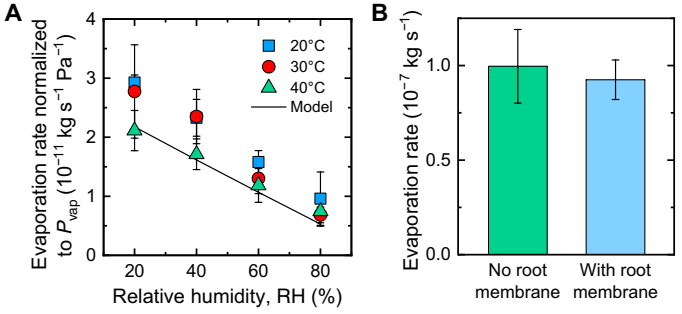

Fig. 2. Evaporation rate of water from the leaves of synthetic mangrove. An AAO membrane comprising nanopores with a diameter of 84 nm was used as the synthetic leaf. Deionized water was used as the feed solution. (**A**) Evaporation rates of pure water from the AAO membrane leaf under different relative humidities (RHs) and temperatures. The evaporation rates measured at each temperature were normalized to the corresponding vapor pressures. Solid line is the normalized evaporation rate, estimated by the convective mass transfer model at each RH and temperature. AAO membrane surface porosity of 40% and air velocity of 0.61 m/s, tangential to the AAO surface, were used in the model (note S2 and table S1). For clarity, only one solid line is plotted as the normalized lines for 20°, 30°, and 40°C were nearly overlaid. (**B**) Evaporation rates of pure water with and without root RO membrane. The evaporation rates were determined at 30°C and 40% relative humidity. Error bars represent ±SD for three different measurements.

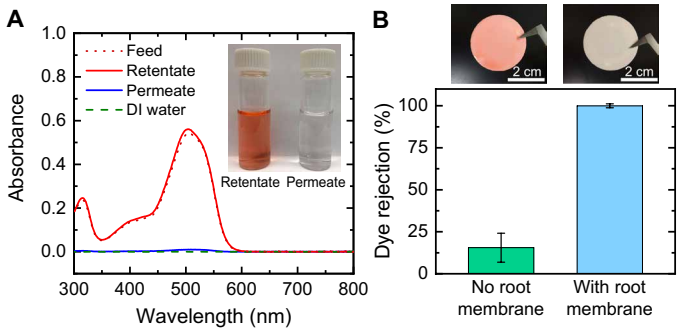

Fig. 3. Rejection of dye molecules by the root membrane under negative pressure. Allura Red dye (1 mM) with Stokes diameter of ~1 nm was used as the feed solution. A commercial RO membrane was used as the root and an AAO membrane with a mean pore diameter of 84 nm was used as the leaf. The dye rejection experiments were performed at 30°C and 40% relative humidity. (**A**) UV-vis spectra of the feed (red dotted), retentate (red), permeate (blue), and deionized (DI) water as a blank (dashed green). The inset shows retentate and permeate solutions after dye rejection experiments. The volume of each vial shown is 2 ml. (**B**) Dye rejection with and without the root membrane. The upper images show the silica frit from the rejection experiments without (left) and with root membrane (right) before dissolution of dye for UV-vis quantification. Error bars represent ±SD for three different measurements. Photo credit: Yunkun Wang, Shandong University, China.

expected pressure drop across the root membrane at the measured water flux is 3.0 bar, meaning that $P_{root} \approx -2$ bar. Thus, when the root RO membrane is installed, positive flux (i.e., flow from the feed reservoir into the synthetic mangrove) typically implies that pressure within the device is slightly negative. Neglecting the pressure drop in the silica frit, the pressure difference at the air/water interface in the AAO leaf should also be 3.0 bar, which would correspond to a contact angle within the nanopores of 85° from Eq. 3.

Exclusion of small dye molecules

After assessing the evaporation rate, we characterized the effectiveness of the root (RO) membrane in excluding small molecules when driven by negative pressure in the synthetic mangrove device. We first colorimetrically evaluated the separating performance of the root membrane by using the anionic dye Allura Red AC (496 g/mol, Stokes diameter of ~1 nm). Water flux through the root membrane was calculated from the evaporation rate, as described above. The silica frit (stem) was used for measurement of the average solute exclusion or rejection, R, defined as $R = 1 - c_{root}/c_o$, where c_{root} and c_o are the solute concentrations in the silica frit and in the feed solution, respectively (*30*). After a defined experimental duration (>30 min of stable flux), dissolution of the contents of the glass frit and root membrane enabled determination of the cumulative solute permeation through the root membrane, which when divided by the total water permeation yielded the average value for c_{root} and, subsequently, the average solute rejection, R.

Ultraviolet-visible (UV-vis) spectroscopy showed that the root membrane effectively excluded the dye (Fig. 3, A and B). Water flux (6.7×10^{-7} m s^{-1}) was similar to that with pure water feed, while dye rejection was 99.97 ± 0.02% (Fig. 3, A and B). In the absence of the root membrane, dye freely entered the silica frit, which resulted in a low observed rejection of 16 ± 9% based on the amount of dye recovered from the frit. The nonzero rejection of dye was due to adsorption by the silica frit. The effective exclusion of dye molecules suggests that the RO membrane remains selective when operating under tension ($P_{root} < P_o \approx 1$ atm), as opposed to the positive hydraulic pressure used in conventional RO operation ($P_o > P_{root} \approx 1$ atm).

Desalination driven by capillarity in nanoporous leaves

The experiments on water evaporation and dye exclusion demonstrated controlled evaporation at the leaf and selective permeation at the root. However, the pressure within the device (P_{root}) was only slightly negative (−2 bar) due to the small osmotic pressures of deionized water ($\pi_o = 0$ bar) and the 1 mM dye solution ($\pi_o = 0.08$ bar). To access larger negative pressures, the synthetic mangrove was used to desalinate aqueous NaCl solutions of increasing concentration. For desalinating conditions (positive water flux paired with salt exclusion), Eq. 2 enables determination of the negative pressure within the system, which is in most cases dominated by the feed osmotic pressure, π_o. As such, π_o is a first approximation of the negative pressure in the system.

We first use AAO membranes with differing, relatively monodisperse nanopores as leaves. The pore size distributions of the two AAO membranes were characterized by scanning electron microscopy (SEM), with Gaussian fits for each AAO membrane yielding mean pore diameters of 84 ± 1 and 215 ± 43 nm (Fig. 4, A and B). The significantly narrower pore size distribution of the smaller-pore-size membrane is evident from the SEM images (Fig. 4, A and B, insets). In addition, the pores themselves were nearly cylindrical and regularly arranged in the 84-nm pore membrane, whereas the 215-nm pore membrane had more irregularly shaped pores. For both membranes, pores fully traverse the membrane thickness, meaning that the general structure is a parallel array of separated, vertical nanochannels.

Water fluxes and salt rejections were evaluated at 30°C and 40% relative humidity for NaCl feed (soil) concentrations varying from 0 to 1 M NaCl (Fig. 4, C and D). For all cases, average water fluxes were obtained by averaging the water fluxes over 1 to 2 hours after an initial ~30-min period of stabilization (fig. S5). The volume of

Downloaded from http://advances.sciencemag.org/ on November 28, 2020

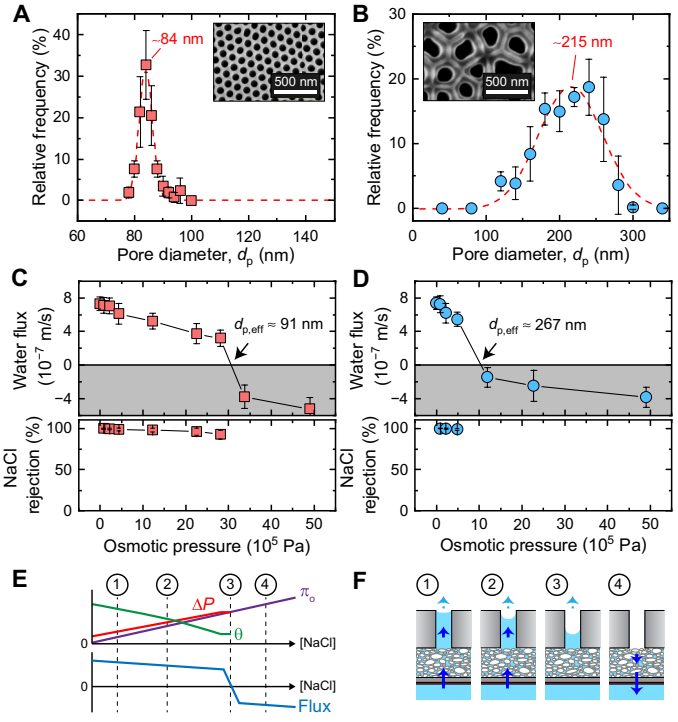

Fig. 4. Water uptake and desalination in the synthetic mangrove. (**A** and **B**) Pore size distributions in two different AAO membranes used as leaves, obtained from image analysis of SEM micrographs (insets). The mean pore diameters from Gaussian fits (dashed red line) for each AAO membrane were identified as 84 ± 1 nm (A) and 215 ± 43 nm (B). Error bars represent ±SD from at least five different SEM micrographs. (**C** and **D**) Water fluxes and salt rejections for AAO membranes with mean pore diameters of 84 nm (C) and 215 nm (D). Here, 0, 0.02, 0.05, 0.1, 0.25, 0.5 (0.6 and 0.7 M NaCl solutions for smaller-diameter AAO membrane experiments), and 1 M NaCl solutions were used as the feed, exerting osmotic pressures ranging from 0 to 49.0 bar. The effective pore diameter, $d_{p,eff}$, for capillarity was estimated from the zero flux points, using the Young-Laplace equation (Eq. 3), to be 91 and 267 nm, respectively. Temperature and relative humidity were set as 30°C and 40%, respectively. (**E**) Mechanistic description of flux behavior, showing the evolution of the feed solution osmotic pressure (π_o, purple line), root pressure difference ($\Delta P = P_o - P_{root}$, red line), water contact angle on the nanopore wall (θ, green line) (Fig. 4D), and water flux across the root membrane (blue line) as NaCl concentration increases in the feed solution. The sign convention of water flux is set as positive if water is withdrawn from the feed solution. (**F**) Anticipated configurations of water level in the synthetic mangrove. The curvature of the water meniscus increases (i.e., θ decreases) as the salt (NaCl) concentration increases to generate sufficient capillary pressure to overcome the osmotic pressure and drive selective water uptake through RO (stages 1 and 2). When the maximum curvature is reached, the osmotic pressure reaches the maximum capillary pressure that is achievable by nanopores of the given diameter (stage 3). Further increase of salt concentration results in negative water flux (i.e., osmosis), with the water level fully retracted from the nanopores (stage 4). Water fluxes in (C) and (D) are calculated from water (liquid) flow rates normalized to the area of RO membrane in the root (1.3×10^{-4} m^2). Error bars represent ±SD for three different measurements.

water that passed through the RO membrane during the stabilization period was comparable to the void volume of the silica frit (0.223 ml). Thus, the stable water fluxes suggest that the water menisci were pinned at the inner surface of AAO nanopores, exerting a consistent negative pressure for water pumping. For the 84-nm pore size AAO membrane leaf, positive fluxes were maintained up to 0.6 M NaCl, corresponding to an osmotic pressure of 28 bar, slightly greater than that of seawater. A synthetic mangrove with this pore-size leaf would therefore be expected to enable capillary-driven desalination of seawater. At greater NaCl concentrations (>0.7 M), the flux reversed, with water flowing from the silica frit of the mangrove device into the feed reservoir. Similar behavior was observed for the AAO membrane leaf with 215-nm pore size, except that positive flux was only maintained up to 0.1 M NaCl with an osmotic pressure of 4.8 bar. The root membrane enabled NaCl rejections above 92% for all cases, with rejection exceeding 98% for salinities below 0.25 M NaCl. Decreased rejections at higher salinities were largely due to the relatively low fluxes in the device, which were roughly 10-fold lower than typical RO fluxes (*37*). Measured rejections agreed well with predicted rejections based on the measured water fluxes and a constant membrane salt permeability (see note S3 and fig. S6). In addition, the salt rejection of RO membranes is affected by ionic strength, with water-salt selectivity typically decreasing at higher salinities, for example, due to decreased electrostatic repulsion (*38*–*41*). No NaCl rejection was observed in the absence of the root membrane (fig. S7).

The flux behavior can be compared with the expected negative pressures based on the Young-Laplace equation. The water contact angle for nonporous aluminum oxide is reported to be 12° (*35*, *36*), which we assume to be similar to the wetting of the AAO pore walls. Inserting this value into Eq. 3 yields the maximum pressure difference ($\Delta P_{max} = P_o - P_{root}$) attainable, which would correspond to the osmotic pressure at which water flux is zero. The osmotic pressures that resulted in zero flux for the two membranes—30.7 and 10.4 bar—correspond to pore diameters of 91 and 267 nm, respectively (Fig. 4, C and D). These values are in good agreement with the mean pore diameters by SEM of 84 and 215 nm, respectively. The agreement is even stronger when considering the polydispersity of the pore sizes; the expected diameters by the Young-Laplace equation (91 and 267 nm) are similar to the highest pore sizes observed by SEM. This suggests that the obtainable negative pressure from an array of nanochannels may be more related to the maximum pore size than the mean pore size.

A mechanistic description of the flux behavior is shown in Fig. 4 (E and F). For increasing feed NaCl concentration, the osmotic pressure of the feed increases nearly linearly. In order for the flux through the root membrane to balance the evaporation rate, the pressure difference ($\Delta P = P_o - P_{root}$) must also increase linearly, meaning that P_{root} decreases at this rate. The negative root pressure (P_{root}) is generated by capillary forces, with the only variable in Eq. 3 being the water contact angle (θ) at the pore wall. With the water-air interface (meniscus) pinned at the pore wall, θ is therefore expected to decrease from near 90° ($P_{root} \approx P_o$) to the minimum water contact angle of 12°, going through stages 1 and 2. At stage 3, an unstable situation occurs in which flux through the root membrane is zero due to the hydraulic pressure matching the osmotic pressure ($\Delta P = \pi_o$), while evaporation at the leaf dries out the pores. Above this unstable point, the AAO membrane leaf is dried, eliminating the generation of negative pressure and resulting in water flux at stage 4 becoming negative due to water being withdrawn by the osmotic pressure difference across the root membrane (i.e., osmosis). This mechanism fully describes the experimental flux behavior, except for the linear decrease in water flux that occurred for increasing π_o. The weak dependency of the water flux on hydraulic pressure in AAO pores predicts the water flux to be nearly constant until stage 3 is reached (see note S4 and fig. S8). We speculate that the decreased flux is due to partial drying (cavitation) in the silica frit or in the AAO membrane leaf, with cavitation exacerbated by the increasingly large negative pressures (*25*).

Downloaded from http://advances.sciencemag.org/ on November 28, 2020

Hydrogel leaf for desalination of hypersaline water

To enable desalination at even larger negative pressures, we developed a hydrogel leaf membrane based on poly(HEMA). A similar chemistry has been used previously in a microfluidic "synthetic tree" to drive water flow using negative pressures approaching −70 bar (*24*). We formed a thin, robust, and permeable hydrogel film by filling the pores of a macroporous polyvinylidene fluoride (PVDF) membrane with a solution of monomer, cross-linker, and photoinitiator, polymerizing under UV irradiation, and immersing the membrane in water (Fig. 5A). The resulting films (table S2) had a thickness of 93 ± 4 μm and a hydraulic pure water permeability of $9 \pm 5 \times 10^{-8}$ m s^{-1} bar^{-1}, ~3-fold lower than the permeability of the root RO membrane. SEM and spectroscopic analyses suggest that the hydrogel completely and uniformly filled the PVDF membrane (figs. S9 to S11).

As with the AAO membrane leaves, capillary-driven water uptake and NaCl rejection were evaluated in the synthetic mangrove with the hydrogel leaf at 30°C and 40% relative humidity (Fig. 5B). The hydrogel leaves allowed for a marked increase in stability compared with the AAO leaves, albeit with a ~60% decrease in water flux at comparable salinities. This difference in water flux suggests that the hydrogel provided meaningful resistance to evaporation (*42*), whereas resistance was minimal in AAO leaves, in which liquid water fills the pores (Figs. 2 and 4). The hydrogel leaf enabled positive flux for all solutions tested, even for a 5 M NaCl solution with an osmotic pressure of 406 bar at 30°C. With a corresponding NaCl rejection of 74%, the hydraulic pressure in the device (P_{root}) was therefore <−338 bar, an enormous negative pressure. For reference, conventional RO is typically limited to a maximum of ~80 bar (*43*).

In addition, the hydrogel leaf allowed for stable operation of at least 48 hours, maintaining relatively constant water flux and salt rejection with feed solutions of 0.1 and 5 M NaCl (Fig. 5C). While performance was relatively steady with no sign of failure, longer measurements were constrained by the finite volume of the mangrove device. In particular, incomplete rejection in the high-salinity experiment allowed for minor salt buildup within the frit. On the basis of the initial RO flux of ~0.3×10^{-7} m/s, the frit volume was filled with permeate solution after ~16 hours. While salt buildup may have affected the longer time points, the relatively stable desalination of hypersaline brine when using the hydrogel leaf was remarkable. In contrast, positive flux abruptly stopped after 6 to 8 hours when using the AAO leaf with 84-nm pore size for feed solutions of 0.05 and 0.5 M NaCl, presumably due to cavitation and embolism in the frit or leaf (fig. S5) (*25*, *44*).

Similar to the AAO leaves, the NaCl rejection decreased with increasing feed osmotic pressure (Fig. 5B). The rejection decrease can again be explained by low water flux (fig. S6) and high salinities (*30*, *39*–*41*, *43*). Design of a device with greater leaf area, relative to the root membrane area, would likely increase the flux and rejection. Other hydrogel materials, particularly polyelectrolytes, could also increase the evaporation rate (*42*, *45*), leading to greater water flux and salt rejection. Neutrally charged hydrogels were used in our study to simplify measurements of salt rejection.

The water flux also decreased with increasing feed osmotic pressure (Fig. 5B). The decreased water flux was transient and feed-dependent, as an equivalent deionized water flux was measured before and after measurements with 5 M NaCl feed (fig. S12). As for the

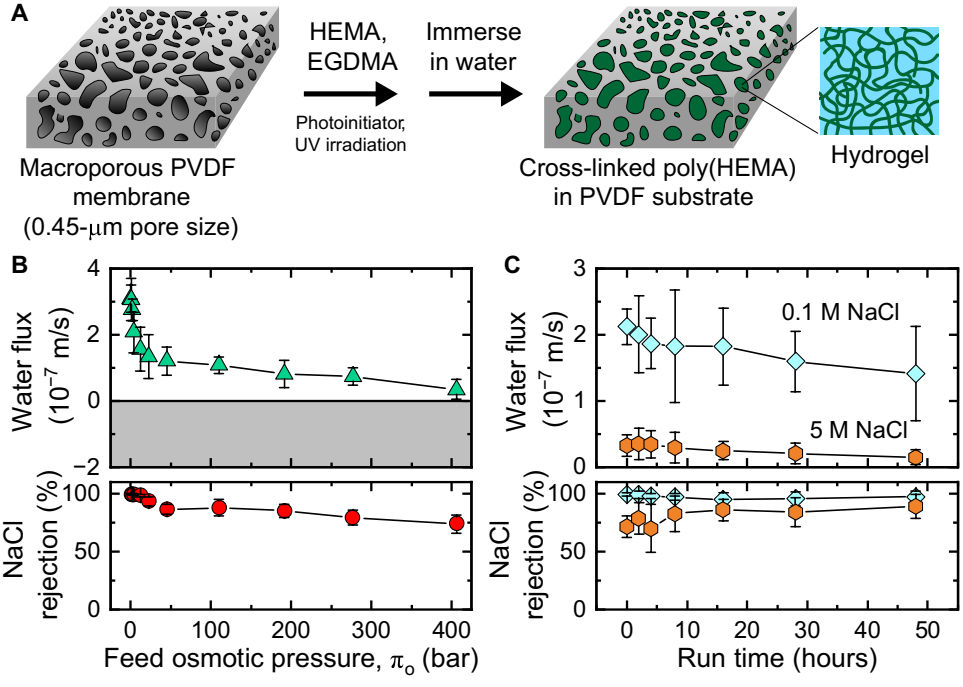

Fig. 5. Desalination of hypersaline solutions and stable water uptake in a synthetic mangrove with a hydrogel leaf. (**A**) Schematic illustration of fabrication of a hydrogel-based synthetic leaf. A robust poly(HEMA) hydrogel film was formed by filling the pores of a macroporous PVDF membrane with monomer solution, polymerizing HEMA with cross-linking by ethylene glycol dimethacrylate (EGDMA) under UV irradiation, and immersing the membrane in water for >24 hours. (**B**) Water fluxes and salt rejections by RO at the root driven by negative pressure in a synthetic mangrove with poly(HEMA) leaves. NaCl solutions with concentrations up to 5 M were used as feed, with corresponding osmotic pressures of up to 406 bar. (**C**) Long-term performance experiment using 0.1 and 5 M NaCl as feed solutions. Temperature and relative humidity were set as 30°C and 40%, respectively. Water fluxes are calculated from water (liquid) flow rates normalized to the area of RO membrane in the root (1.3×10^{-4} m^2). Error bars represent ±SD for three different measurements.

Downloaded from http://advances.sciencemag.org/ on November 28, 2020

AAO membrane leaves, the decrease in water flux with increasing osmotic pressure was greater than expected for the hydrogel leaf. From the solution-diffusion model, assuming constant diffusivity through the hydrogel thickness, a nearly linear, modest decrease in water flux is expected (see derivation in note S5 and figs. S12 and S13). However, water diffusivity in hydrogels is exponentially dependent on the water content (*39*, *46*). Modeling of a similar hydrogel system suggested that evaporation causes a sharp decrease in the water content near the hydrogel/gas interface, leading to an even sharper decrease in the local water diffusivity (*42*). If negative pressure further decreases the water content within the hydrogel leaf, then this may explain the drop in flux. Cavitation and partial embolism in the silica frit may also have played a role, as discussed earlier for the AAO leaves (*25*, *44*).

DISCUSSION

Our work unequivocally demonstrated capillary-driven, selective desalination of saline (and hypersaline) water under large negative pressures, directly supporting the applicability of the cohesion-tension theory to desalination and long-range water transport in mangroves. The synthetic mangrove device could be used to further study transpiration and desalination in mangroves, particularly to assess the impact of other leaf, stem (xylem), and root structures on flow, selectivity, and resistance to cavitation. In addition, the synthetic mangrove device allowed for stable operation at unprecedented negative pressures (<−338 bar). Susceptibility to cavitation is ultimately the main limitation of capillary-driven devices. The synthetic mangrove allowed for stable desalination, even without the structural complexity of natural xylems (e.g., pit membranes), let alone the ability of plants to refill xylem chambers in which cavitation has occurred (*1*, *13*). The relatively high stability in the synthetic mangrove compared with many other engineered devices may be attributed to (i) its hydrophilic, porous stem (silica frit) with small pore sizes (<10 μm) and (ii) the presence of selective membranes at both the root and leaf, which hinder the entry of impurities that could induce cavitation. Similar stability was observed in the all-hydrogel synthetic tree, where the entire device was essentially a low-permeability membrane (*24*). The stable operation of the synthetic mangrove suggests a new, general format for devices with capillary-driven flow, wherein thin, selective membranes stabilize the region of negative pressure from the ambient environment, and a porous hydrophilic structure allows for low-resistance, long-range water convection at negative pressures. The particle size of the hydrophilic structure could be tailored to provide adequate permeability (large particles) and resistance to cavitation (small particles), depending on the needs of the device.

Desalination is a critically important tool to produce fresh water from nontraditional sources. In mangrove trees and the synthetic mangrove, the energy for desalination and translocation of water comes mainly through heat absorption from the environment to induce evaporation. In large industrial systems, however, the energy for evaporation would need to be supplied, as is already the case in thermal desalination facilities (*8*, *37*). For this reason, capillary-driven desalination is likely not a feasible alternative for large-scale desalination applications. Instead, we envision that synthetic mangrove devices could be integrated into urban infrastructure for passive stormwater management. For example, buildings could be modeled as de facto synthetic mangrove devices to decrease flooding damage, as part of the "sponge city" concept (*47*). In this scenario, the buildings themselves would soak up excess groundwater and evaporate the water from their walls and roofs. Hydrophilic films (e.g., hydrogels) on the building exterior would serve as sites for evaporation and generation of negative pressure. A hydrophilic porous wall structure would allow for long-range transport of metastable water. At the base of the building, a selective membrane would mitigate cavitation and block particulate matter while removing excess water from the ground. The evaporation of water from the building walls would additionally provide passive cooling.

Other potential applications of the synthetic mangrove device include microfluidic and off-grid devices, such as environmental sensors. Providing electrical energy to drive high-pressure flow could be a major limitation for some sensors. Capillary-driven flow would overcome this limitation. For example, negative pressure could be used to drive high-performance liquid chromatography in a sensing device, with thermal energy from the environment driving both fluid flow and molecular separation, as in the natural mangrove. Electrical energy would be needed only for the embedded detector. The selectivity of the root membrane could also be tailored for the desired application, with the membrane filtering out contaminant species or even performing the chromatographic separation itself.

MATERIALS AND METHODS

Setup of the synthetic mangrove and flux measurements

The setup of the synthetic mangrove is illustrated in Fig. 1 and fig. S1. The experimental cell with dimensions of 62 mm by 45 mm by 24 mm was homemade using cast acrylic (McMaster-Carr). The synthetic mangrove cell as shown comprises a glass syringe (250 μl, Hamilton), feed reservoir (7.5 ml), 28-mm diameter porous AAO membrane (Hefei Pu-Yuan Nanotechnology Ltd.) or 30-mm diameter hydrogel film, 30-mm diameter silica frit with 0.9- to 1.4-μm nominal pore size and 2.2-mm thickness (ACE Glass), and seawater RO membrane (SW30HR, Dow Water & Process Solutions). Silicone O-rings (McMaster-Carr) were used to prevent leakage. After sealing with the O-rings, the effective membrane diameters were 12.7 mm (1.3×10^{-4} m^2 area), 28 mm (6.2×10^{-4} m^2 area), and 30 mm (7.1×10^{-4} m^2 area) for the root RO membrane, AAO leaf membrane, and poly(HEMA) leaf membrane, respectively.

For flux measurements, the device was assembled with components (silica frit and leaf membrane) prewetted in deionized water, after which deionized water was added to the feed reservoir. After the evaporation rate stabilized (~30 min), the deionized water solution was quickly replaced with the desired feed solution. A graduated glass syringe mounted on the feed reservoir was used to measure the water volume change. A camera (WideCam F100, Genius) acquired images of the syringe at designated time intervals, from which the volume change was analyzed. Flux was recorded only after the flux was stable for >30 min. Typically, over the course of an experiment, the liquid volume in the feed reservoir (initial volume of 7.5 ml) decreased <0.5 ml, which led to relatively small increases in the osmotic pressure of the feed NaCl solutions over time. All experiments were performed in a custom closed chamber, in which the temperature (20°, 30°, and 40°C) and relative humidity (20, 40, 60, and 80%) were controlled by a microprocessor controller (Electro-Tech Systems Inc.). The velocity of air in the chamber was measured using a velocity meter (Vaneometer, Dwyer, Instruments Inc.). Immediately before experiments, the silica frit and AAO membranes were

Downloaded from http://advances.sciencemag.org/ on November 28, 2020

cleaned by air plasma for 10 min in a plasma cleaner (PDC-32G, Harrick Plasma) at 14 W and ~0.7 mtorr. During the experiments, the mangrove cell was placed on a magnetic stirrer, and the solution in the feed reservoir was constantly mixed by a stir bar (10 mm × 13 mm) at 450 rpm. Each experimental condition was repeated three times.

Dye and salt rejection tests

For root solute rejection tests, 1 mM Allura Red AC dye (496 g/mol, 80%; Sigma-Aldrich) and different concentrations of NaCl solutions were used as feed solutions. During the filtration experiments, the volume change was monitored for calculation of water flux. After filtration experiments, the mangrove cell was disassembled, and the silica frit and SW30HR membrane were immersed into 10 ml of deionized water for 2 hours to dissolve the contents of the frit and membrane, after which the solute concentration was measured. Dye concentration was quantified by absorbance at 500 nm in a UV-vis spectrometer (Cary 50 Bio). NaCl concentration was quantified by measuring electrical conductivity with a calibrated conductivity meter (CON2700, Oakton). Solute rejection was then calculated by mass balance. The osmotic pressures of NaCl solutions were calculated using the software OLI (OLI systems, Hanover, NJ).

Hydrogel membrane fabrication

2-Hydroxyethyl methacrylate (monomer, 97%; Sigma-Aldrich) was mixed with ethylene glycol dimethacrylate (EGDMA; crosslinker, 98%; Sigma-Aldrich) and 4,4′-azobis(4-cyanovaleric acid) (ACVA; photoinitiator, 98%; Sigma-Aldrich) to form the reaction solution (HEMA/EGDMA/ACVA = 100:10:0.5 by weight) (*48*). To provide mechanical robustness, composite hydrogel films were formed within a macroporous PVDF membrane with 0.45-μm nominal pore size (Hydrophobic Durapore, Merck Millipore Ltd.). The reaction mixture was added to the PVDF membrane, which was then sealed between two glass slides. The sample was then immediately photopolymerized by exposure to 364-nm UV light (0.5 hours for both sides) at room temperature to form a solid composite film. After removing the glass slides, the film was immersed in deionized water for 24 hours to remove residual unreacted chemicals and allow for water penetration. The films were stored in deionized water before use.

AAO pore size characterization

The surface morphology of AAO membranes was characterized by SEM (Hitachi SU-70, Hitachi High Technologies America Inc.) at 15.0 kV and a 5.0-mm working distance. Samples were coated with iridium (8-nm thickness) using a Cressington Sputter Coater 208HR at a current of 40 mA. AAO surface porosity was estimated by SEM imaging of randomly selected membrane regions followed by analysis in ImageJ. Effective diameters of the individual nanopores were calculated by assuming a circular pore with the same cross-sectional area as a given nanopore. SEM images were taken at five and seven random locations for the 84- and 215-nm pore size membranes, respectively. For each AAO membrane type, all membranes analyzed by SEM and used in experiments originated from the same manufacturing batch. Pores observed in the SEM images are therefore representative of the pore sizes encountered in our experiments. The observed frequencies of each pore-size bin were averaged across the SEM images to obtain the pore size histograms in Fig. 4.

SUPPLEMENTARY MATERIALS

Supplementary material for this article is available at http://advances.sciencemag.org/cgi/content/full/6/8/eaax5253/DC1

Note S1. Pressure drop across silica frit.
Note S2. Water evaporation rate measurements and calculations.
Note S3. Hydrogel and RO membrane characterization.
Note S4. Dependency of water flux on hydraulic pressure in AAO nanopores.
Note S5. Derivation of water flux through the hydrogel leaf.
Fig. S1. Photograph of the synthetic mangrove.
Fig. S2. SEM images of silica frit.
Fig. S3. On-line water level monitoring system.
Fig. S4. Vapor concentration boundary layer on the AAO membrane.
Fig. S5. Initially stable flux followed by total loss of flux for AAO membranes with mean pore diameters of 84 nm as leaves.
Fig. S6. Correlation between water flux and NaCl rejection.
Fig. S7. Water flux and NaCl rejection without RO membrane root as a function of feed solution osmotic pressure.
Fig. S8. Schematic of AAO pores, water meniscus, and vapor concentration boundary layer.
Fig. S9. SEM images and energy dispersive x-ray spectroscopy (EDS) line scan profiles on the cross sections of PVDF and PVDF-poly(HEMA) membranes.
Fig. S10. Infrared spectroscopy of PVDF microporous membrane and poly(HEMA) hydrogel in PVDF substrate.
Fig. S11. X-ray photoelectron spectroscopy (XPS) characterization of hydrogel-based leaf.
Fig. S12. Impact of feed concentration on evaporative water flux from poly(HEMA) hydrogel leaf.
Fig. S13. Modeled profiles for water flux through the hydrogel-based leaf membrane.
Table S1. Properties of anodic aluminum oxide (AAO) isotropic membrane filters.
Table S2. Properties of poly(HEMA)-based hydrogel.
References (*49*–*52*)

REFERENCES AND NOTES

1. R. Reef, C. E. Lovelock, Regulation of water balance in mangroves. *Ann. Bot.* **115**, 385–395 (2015).
2. C. Paliyavuth, B. Clough, P. Patanaponpaiboon, Salt uptake and shoot water relations in mangroves. *Aquat. Bot.* **78**, 349–360 (2004).
3. M. A. Sobrado, Influence of external salinity on the osmolality of xylem sap, leaf tissue and leaf gland secretion of the mangrove *Laguncularia racemosa* (L.) Gaertn. *Trees* **18**, 422–427 (2004).
4. P. Krishnamurthy, P. A. Jyothi-Prakash, L. Qin, J. He, Q. Lin, C.-S. Loh, P. P. Kumar, Role of root hydrophobic barriers in salt exclusion of a mangrove plant *Avicennia officinalis*. *Plant Cell Environ.* **37**, 1656–1671 (2014).
5. J. N. Israelachvili, *Intermolecular and Surface Forces* (Elsevier, Amsterdam, 2011), pp. 674.
6. H. Sui, B.-G. Han, J. K. Lee, P. Walian, B. K. Jap, Structural basis of water-specific transport through the AQP1 water channel. *Nature* **414**, 872–878 (2001).
7. M. Popp, J. Polania, M. Weiper, in *Towards the Rational use of High Salinity Tolerant Plants*, H. Lieth, A. A. Al Masoom, Eds. (Springer Netherlands, Dordrecht, 1993), Vol. 1 Deliberations about High Salinity Tolerant Plants and Ecosystems, pp. 217–224.
8. M. Elimelech, W. A. Phillip, The future of seawater desalination: Energy, technology, and the environment. *Science* **333**, 712–717 (2011).
9. M. A. Shannon, P. W. Bohn, M. Elimelech, J. G. Georgiadis, B. J. Mariñas, A. M. Mayes, Science and technology for water purification in the coming decades. *Nature* **452**, 301–310 (2008).
10. Y. Waisel, A. Eshel, M. Agami, Salt balance of leaves of the mangrove *Avicennia-Marina*. *Physiol. Plant.* **67**, 67–72 (1986).
11. M. W. Vandegehuchte, A. Guyot, M. Hubau, S. R. E. De Groote, N. J. F. De Baerdemaeker, M. Hayes, N. Welti, C. E. Lovelock, D. A. Lockington, K. Steppe, Long-term versus daily stem diameter variation in co-occurring mangrove species: Environmental versus ecophysiological drivers. *Agric. For. Meteorol.* **192–193**, 51–58 (2014).
12. P. F. Scholander, E. D. Bradstreet, E. A. Hemmingsen, H. T. Hammel, Sap pressure in vascular plants: Negative hydrostatic pressure can be measured in plants. *Science* **148**, 339–346 (1965).
13. A. D. Stroock, V. V. Pagay, M. A. Zwieniecki, N. M. Holbrook, The physicochemical hydrodynamics of vascular plants. *Annu. Rev. Fluid Mech.* **46**, 615–642 (2014).
14. M. T. Tyree, Plant hydraulics: The ascent of water. *Nature* **423**, 923 (2003).
15. J. S. Sperry, in *Mechanical Integration of Plant Cells and Plants*, P. Wojtaszek, Ed. (Springer, 2011), vol. 9, pp. 303–327.
16. J. S. Sperry, M. T. Tyree, Mechanism of water stress-induced xylem embolism. *Plant Physiol.* **88**, 581–587 (1988).
17. W. T. Pockman, J. S. Sperry, J. W. O'Leary, Sustained and significant negative water-pressure in xylem. *Nature* **378**, 715–716 (1995).

Downloaded from http://advances.sciencemag.org/ on November 28, 2020

18. N. Goedecke, J. Eijkel, A. Manz, Evaporation driven pumping for chromatography application. *Lab Chip* **2**, 219–223 (2002).
19. G. M. Walker, D. J. Beebe, A passive pumping method for microfluidic devices. *Lab Chip* **2**, 131–134 (2002).
20. G. M. Walker, D. J. Beebe, An evaporation-based microfluidic sample concentration method. *Lab Chip* **2**, 57–61 (2002).
21. O. Vincent, A. Szenicer, A. D. Stroock, Capillarity-driven flows at the continuum limit. *Soft Matter* **12**, 6656–6661 (2016).
22. R. T. Borno, J. D. Steinmeyer, M. M. Maharbiz, Charge-pumping in a synthetic leaf for harvesting energy from evaporation-driven flows. *Appl. Phys. Lett.* **95**, 013705 (2009).
23. K. Kim, H. Kim, J. H. Lim, S. J. Lee, Development of a desalination membrane bioinspired by mangrove roots for spontaneous filtration of sodium ions. *ACS Nano* **10**, 11428–11433 (2016).
24. T. D. Wheeler, A. D. Stroock, The transpiration of water at negative pressures in a synthetic tree. *Nature* **455**, 208–212 (2008).
25. C. Duan, R. Karnik, M.-C. Lu, A. Majumdar, Evaporation-induced cavitation in nanofluidic channels. *Proc. Natl. Acad. Sci. U.S.A.* **109**, 3688–3693 (2012).
26. H. J. Schenk, K. Steppe, S. Jansen, Nanobubbles: A new paradigm for air-seeding in xylem. *Trends Plant Sci.* **20**, 199–205 (2015).
27. N. R. Tas, P. Mela, T. Kramer, J. W. Berenschot, A. van den Berg, Capillarity induced negative pressure of water plugs in nanochannels. *Nano Lett.* **3**, 1537–1540 (2003).
28. C. R. Brodersen, A. J. McElrone, B. Choat, M. A. Matthews, K. A. Shackel, The dynamics of embolism repair in xylem: In vivo visualizations using high-resolution computed tomography. *Plant Physiol.* **154**, 1088–1095 (2010).
29. K. Kim, E. Seo, S.-K. Chang, T. J. Park, S. J. Lee, Novel water filtration of saline water in the outermost layer of mangrove roots. *Sci. Rep.* **6**, 20426 (2016).
30. R. W. Baker, *Membrane Technology and Applications* (John Wiley & Sons, Ltd, 2012), pp. 575.
31. J. G. Wijmans, R. W. Baker, The solution-diffusion model: a review. *J. Membr. Sci.* **107**, 1–21 (1995).
32. J. R. Werber, C. O. Osuji, M. Elimelech, Materials for next-generation desalination and water purification membranes. *Nat. Rev. Mater.* **1**, 16018 (2016).
33. C. E. Lovelock, M. C. Ball, B. Choat, B. M. J. Engelbrecht, N. M. Holbrook, I. C. Feller, Linking physiological processes with mangrove forest structure: Phosphorus deficiency limits canopy development, hydraulic conductivity and photosynthetic carbon gain in dwarf *Rhizophora mangle*. *Plant Cell Environ.* **29**, 793–802 (2006).
34. B. Choat, A. R. Cobb, S. Jansen, Structure and function of bordered pits: new discoveries and impacts on whole-plant hydraulic function. *New Phytol.* **177**, 608–626 (2008).
35. K. P. Lee, H. Leese, D. Mattia, Water flow enhancement in hydrophilic nanochannels. *Nanoscale* **4**, 2621–2627 (2012).
36. D. Megias-Alguacil, E. Tervoort, C. Cattin, L. J. Gauckler, Contact angle and adsorption behavior of carboxylic acids on α-Al2O3surfaces. *J. Colloid Interface Sci.* **353**, 512–518 (2011).
37. L. F. Greenlee, D. F. Lawler, B. D. Freeman, B. Marrot, P. Moulin, Reverse osmosis desalination: Water sources, technology, and today's challenges. *Water Res.* **43**, 2317–2348 (2009).
38. S. Bason, Y. Oren, V. Freger, Ion transport in the polyamide layer of RO membranes: Composite membranes and free-standing films. *J. Membr. Sci.* **367**, 119–126 (2011).
39. G. M. Geise, D. R. Paul, B. D. Freeman, Fundamental water and salt transport properties of polymeric materials. *Prog. Polym. Sci.* **39**, 1–42 (2014).
40. A. P. Straub, C. O. Osuji, T. Y. Cath, M. Elimelech, Selectivity and mass transfer limitations in pressure-retarded osmosis at high concentrations and increased operating pressures. *Environ. Sci. Technol.* **49**, 12551–12559 (2015).
41. C. Bartels, R. Franks, S. Rybar, M. Schierach, M. Wilf, The effect of feed ionic strength on salt passage through reverse osmosis membranes. *Desalination* **184**, 185–195 (2005).
42. F. Fornasiero, D. Tang, A. Boushehri, J. Prausnitz, C. J. Radke, Water diffusion through hydrogel membranes: A novel evaporation cell free of external mass-transfer resistance. *J. Membr. Sci.* **320**, 423–430 (2008).
43. D. M. Davenport, A. Desmukh, J. R. Werber, M. Elimelech, High-pressure reverse osmosis for energy-efficient hypersaline brine eesalination: Current status, design considerations, and research needs. *Environ. Sci. Technol. Lett.* **5**, 467–475 (2018).
44. M. T. Tyree, J. S. Sperry, Vulnerability of xylem to cavitation and embolism. *Annu. Rev. Plant. Physiol. Plant. Mol. Biol.* **40**, 19–36 (1989).
45. M. F. Refojo, H. Yasuda, Hydrogels from 2-hydroxyethyl methacrylate and propylene glycol monoacrylate. *J. Appl. Polym. Sci.* **9**, 2425–2435 (1965).
46. H. Yasuda, C. E. Lamaze, L. D. Ikenberry, Permeability of solutes through hydrated polymer membranes. Part I. Diffusion of sodium chloride. *Makromol. Chem.* **118**, 19–35 (1968).
47. Y. Jiang, C. Zevenbergen, Y. Ma, Urban pluvial flooding and stormwater management: A contemporary review of China's challenges and "sponge cities" strategy. *Environ. Sci. Policy* **80**, 132–143 (2018).
48. X. Lu, X. Feng, J. R. Werber, C. Chu, I. Zucker, J.-H. Kim, C. O. Osuji, M. Elimelech, Enhanced antibacterial activity through the controlled alignment of graphene oxide nanosheets. *Proc. Natl. Acad. Sci. U.S.A.* **114**, E9793–E9801 (2017).
49. J. H. Lienhard, J. H. Lienhard, *A Heat Transfer Textbook* (Dover Publications, Mineola, N.Y., ed. 4, 2011), pp. 755.
50. T. R. Marrero, E. A. Mason, Gaseous diffusion coefficients. *J. Phys. Chem. Ref. Data* **1**, 3–118 (1972).
51. J. R. Werber, A. Deshmukh, M. Elimelech, The critical need for increased selectivity, not increased water permeability, for desalination membranes. *Environ. Sci. Technol. Lett.* **3**, 112–120 (2016).
52. H. Ju, A. C. Sagle, B. D. Freeman, J. I. Mardel, A. J. Hill, Characterization of sodium chloride and water transport in crosslinked poly(ethylene oxide) hydrogels. *J. Membr. Sci.* **358**, 131–141 (2010).

Acknowledgments: We thank E. Shaulsky and X. Zhou from the Yale Department of Chemical and Environmental Engineering for helping to make the synthetic mangrove device and characterize the poly(HEMA) hydrogel, respectively; F. Zheng from the Shandong University for help in conducting stability experiments; and C. Brodersen from the Yale School of Forestry and Environmental Studies for helpful discussion. **Funding:** We acknowledge the support received from the National Natural Science Foundation of China (NSFC, 51878389) and the National Science Foundation through the Engineering Research Center for Nanotechnology-Enabled Water Treatment (EEC-1449500). Y.W. is grateful for the support from the China Scholarship Council postdoctoral fellowship. J.L. acknowledges funding support from the Natural Sciences and Engineering Research Council of Canada (NSERC) through the Discovery Grant. **Author contributions:** J.L. conceived the idea. Y.W., J.R.W., and J.L. designed and performed the experiments and analyzed the data. All authors discussed the results and wrote the manuscript. **Competing interests:** The authors declare that they have no competing interests. **Data and materials availability:** All data needed to evaluate the conclusions in the paper are present in the paper and/or the Supplementary Materials. Additional data related to this paper may be requested from the authors.

Submitted 31 March 2019
Accepted 26 November 2019
Published 21 February 2020
10.1126/sciadv.aax5253

Citation: Y. Wang, J. Lee, J. R. Werber, M. Elimelech, Capillary-driven desalination in a synthetic mangrove. *Sci. Adv.* **6**, eaax5253 (2020).

Downloaded from http://advances.sciencemag.org/ on November 28, 2020

Science Advances

Capillary-driven desalination in a synthetic mangrove

Yunkun Wang, Jongho Lee, Jay R. Werber and Menachem Elimelech

Sci Adv **6** (8), eaax5253.
DOI: 10.1126/sciadv.aax5253

ARTICLE TOOLS http://advances.sciencemag.org/content/6/8/eaax5253

SUPPLEMENTARY MATERIALS http://advances.sciencemag.org/content/suppl/2020/02/14/6.8.eaax5253.DC1

REFERENCES This article cites 47 articles, 6 of which you can access for free
http://advances.sciencemag.org/content/6/8/eaax5253#BIBL

PERMISSIONS http://www.sciencemag.org/help/reprints-and-permissions

Use of this article is subject to the Terms of Service

Science Advances (ISSN 2375-2548) is published by the American Association for the Advancement of Science, 1200 New York Avenue NW, Washington, DC 20005. The title *Science Advances* is a registered trademark of AAAS.

Copyright © 2020 The Authors, some rights reserved; exclusive licensee American Association for the Advancement of Science. No claim to original U.S. Government Works. Distributed under a Creative Commons Attribution NonCommercial License 4.0 (CC BY-NC).

Downloaded from http://advances.sciencemag.org/ on November 28, 2020